

Nuclear shape dynamics in low-energy heavy-ion reactions

Kouichi Hagino^{1,2,3}

¹Department of Physics, Kyoto University, Kyoto 606-8502, Japan

²Institute for Liberal Arts and Sciences, Kyoto University, Kyoto 606-8501, Japan

³RIKEN Nishina Center for Accelerator-based Science, RIKEN, Wako 351-0198, Japan

Abstract. We discuss recent theoretical developments in low-energy heavy-ion reactions. To this end, we put emphasis on a viewpoint of probing nuclear shapes with heavy-ion reactions. We first discuss a single-channel problem with an optical potential model. We particularly discuss a microscopic modeling of the imaginary part of an optical potential as well as a visualization of quantum interference phenomena observed in heavy-ion elastic scattering. We then discuss multi-channel scattering problems, and demonstrate that heavy-ion fusion reactions at energies around the Coulomb barrier are sensitive to the shape of colliding nuclei, providing a powerful tool to probe nuclear shapes. We finally point out that relativistic heavy-ion collisions have large similarities to low-energy heavy-ion reactions in the context of nuclear shape dynamics.

1 Introduction

A goal of low-energy nuclear physics is to understand atomic nuclei as quantum many-body systems of nucleons, that is, to understand several properties of nuclei in terms of nucleon degrees of freedom. These can be mainly divided into two categories: the first category concerns static properties of atomic nuclei, such as the mass, the size, the shape, and excitations of atomic nuclei, while the second category deals with their dynamical properties. These are covered by nuclear structure physics and nuclear reaction physics, respectively. Of course, there is no clear separation between these two. As a matter of fact, one of the most important roles of nuclear reactions is to serve as a tool to investigate nuclear structure. For instance, by knocking out a nucleon from a nucleus using nuclear reactions, one can learn single-particle natures of nuclei [1]. Three-body scattering, such as the $d+p$ reaction, has been utilized to investigate a three-nucleon interaction [2]. Furthermore, heavy-ion fusion reactions have been used as a standard tool to synthesize superheavy elements [3, 4].

Besides this aspect, nuclear reaction has another aspect. That is, the reaction dynamics itself is rich and complex, making it an interesting topics to study. Good examples for this include a formation of a compound nucleus with neutron induced reactions and its relation to quantum chaos [5], dynamics of the pre-equilibrium process towards a compound nucleus [6], and heavy-ion fusion reactions as quantum tunneling phenomena with many degrees of freedom [7, 8].

In this contribution, we shall discuss both of these aspects of nuclear reactions. For the latter aspect, we shall discuss quantum interference phenomena observed in nuclear reactions. We shall also introduce a novel method to visualize the quantum interferences by taking the Fourier

transform of the scattering amplitude. For the former aspect, we shall mainly focus on extracting nuclear shapes from nuclear reactions. In passing, the richness of nuclear reaction dynamics originates from the fact that a nucleus is a composite system. If a nucleus was a point particle, only elastic scattering took place. However, in reality, because of the many-body nature of a nucleus, there exist rich reaction processes, including not only elastic scattering but also inelastic scattering, particle transfer reactions, and fusion reactions. These nuclear reaction processes are not independent with each other, but they significantly affect one another. For instance, the ground state properties of colliding nuclei, such as the shape of the nuclei as well as their excitations, significantly affect those nuclear reaction processes [7, 8]. Using this property, information on nuclear deformation has been successfully extracted for several nuclei from low-energy heavy-ion fusion reactions [9]. In recent years, a similar idea has been employed in relativistic heavy-ion collisions as well, providing an interesting intersection between low-energy and high-energy heavy-ion reactions [10, 11]. We shall also discuss this topic in this contribution.

2 Single-channel problems

2.1 Microscopic modeling of the imaginary part of an optical potential

Let us start with the simplest model of nuclear reactions, that is, single-channel scattering with an optical potential. An optical potential is a complex potential given by,

$$V_{\text{opt}}(r) = V(r) - iW(r), \quad (1)$$

where r is the relative coordinate between two colliding nuclei. This model can describe either elastic scattering

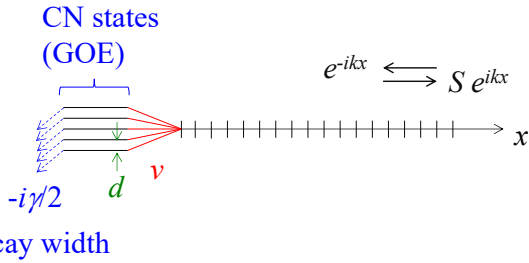


Figure 1. A schematic illustration of the schematic model proposed in Ref. [15] for a microscopic modeling of an imaginary part of an optical potential. In this model, the entrance channel Hamiltonian in the discrete basis representation couples to compound nucleus states described with the random matrix based on the Gaussian Orthogonal Ensemble (GOE). γ and d are the decay width and the mean level spacing of the compound nucleus states, respectively.

or absorption processes. The imaginary part of the optical potential causes a loss of the flux, thus the absorption, which is originated from reaction processes other than elastic scattering, such as inelastic scattering, transfer reactions, and fusion reactions. In this approach, the dynamics after absorption is treated as a black box.

On the other hand, there are several reaction processes in which the dynamics after the absorption is important. These include fusion of superheavy nuclei and fusion of two ^{12}C nuclei. For the former, a re-separation process after the touching, referred to as quasi-fission, plays a crucial role [12]. On the other hand, for the latter, the astrophysical S -factor for the $^{12}\text{C} + ^{12}\text{C}$ system exhibits several prominent resonance structures in contrast to those for the $^{12}\text{C} + ^{13}\text{C}$ system, which show a much smoother energy dependence [13]. It was argued in Ref. [14] that the different behaviors of fusion cross sections, and thus the astrophysical S -factors, in these systems are caused by different properties of the compound nuclei, ^{24}Mg and ^{25}Mg , indicating that the resonances are isolated in the $^{12}\text{C} + ^{12}\text{C}$ fusion reaction at low energies, while the $^{12}\text{C} + ^{13}\text{C}$ fusion reaction lies in the overlapping resonance regime.

To understand the underlying mechanism of the fusion reactions of the carbon isotopes, we recently constructed a simple schematic model, which consists of a random matrix Hamiltonian based on the Gaussian Orthogonal Ensemble (GOE) [15]. See Fig. 1 for a schematic illustration of the model. Each of the GOE configurations possesses a decay width γ so that a part of the incident flux is absorbed by the GOE configurations. As a result, the absolute value of the S -matrix becomes less than one, $|S| < 1$. This is how the imaginary part of the optical potential is modeled in this approach. By changing the interaction strength in the GOE Hamiltonian, one can control the level density ρ of a "compound nucleus". Figure 2 shows the transmission coefficients for two different model parameters. The blue dashed line shows the transmission coefficient for $\gamma/d = 20$, where $d = 1/\rho$ is the mean level spacing. In this case, the transmission coefficients are close to unity, that is consistent with the strong absorption limit. On the

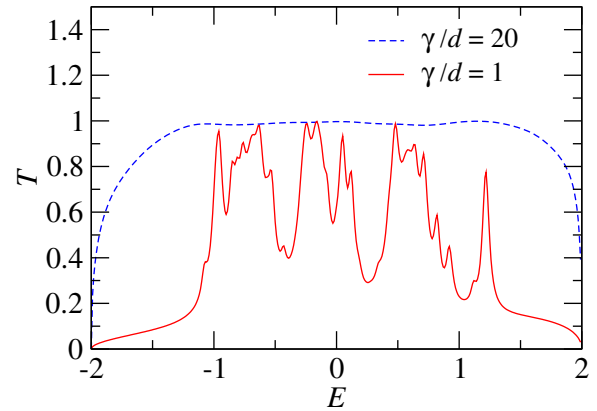


Figure 2. Transmission coefficients T as a function of the incident energy E obtained with the schematic model introduced in Ref. [15] (see Fig. 1). The blue dashed line is for $\gamma/d = 20$, while the red solid line for $\gamma/d = 1$.

other hand, the red solid line shows the transmission coefficients for $\gamma/d = 1$, for which the transmission coefficients are much more structured as a function of E with several prominent resonance peaks. It is interesting to observe that the transmission coefficients are close to unity at a few resonance energies, being consistent with the experimental observations in the C+C fusion reactions.

2.2 Imaging quantum interference phenomena in heavy-ion elastic scattering

One of the interesting aspects in low-energy heavy-ion reactions is that various quantum interference phenomena are seen in their differential cross sections. A textbook example for this is scattering of two identical particles, referred to as Mott scattering. For such scattering, a detector cannot distinguish scattering at angle θ from scattering at angle $\pi - \theta$, causing the characteristic interference pattern in the angular distribution [16]. Another example is the nearside-farside interference [17], in which the nearside component corresponds to scattering with a positive impact parameter while the farside component is associated with a negative impact parameter. Notice that scattering takes place only at the edges of a nucleus due to a strong absorption inside a nucleus. The nearside and the farside components correspond to scattering at the opposite sides of the edges, and thus has a close analogy to scattering through two slits in the double slit problem [17].

These quantum interference phenomena can be described with an optical potential, Eq. (1). Using the optical potential, one can construct the scattering amplitude $f(\theta)$ e.g., with the partial wave decomposition technique, from which the differential cross sections $d\sigma/d\Omega$ can be computed as $d\sigma/d\Omega = |f(\theta)|^2$. By decomposing the scattering amplitude $f(\theta)$ into two or more components, $f(\theta) = \sum_i f_i(\theta)$, one can obtain the interferences among the different components of the scattering amplitude.

We would like to ask a question here: what would happen if one takes the Fourier transform of the scattering am-

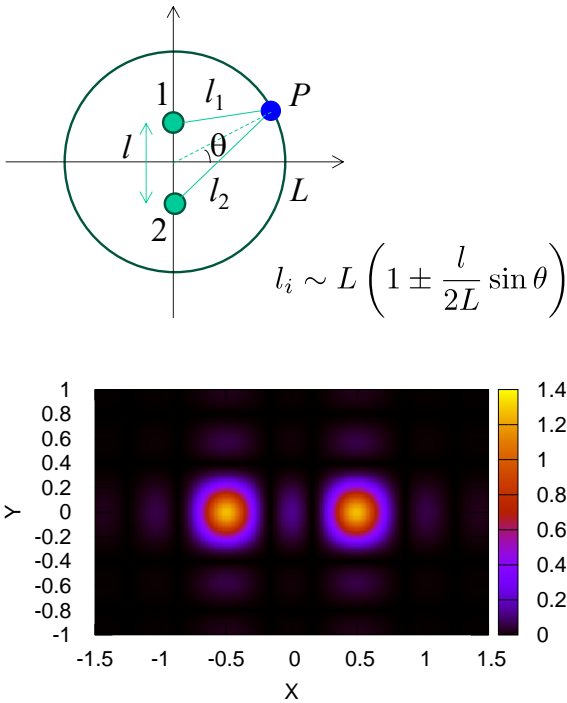


Figure 3. (Upper panel) A schematic illustration of a setup of the double-slit problem. (Lower panel) The imaging of the double-slit problem with Eq. (2) on the two-dimensional (X, Y) plane. The parameters are taken to be $l = 1, k = 30, \theta_0 = 0$, and $\Delta\theta = \Delta\varphi = 15$ degree.

plitude, $f(\theta)$? That is,

$$\Phi(X, Y) \propto \int_{\theta_0-\Delta\theta}^{\theta_0+\Delta\theta} d\theta \int_{-\Delta\varphi}^{\Delta\varphi} d\varphi e^{ik(\theta X + \varphi Y)} f(\theta). \quad (2)$$

Let us first consider a double slit problem with classical waves with the amplitude A , the wave length λ , and the angular frequency ω . For this problem, the total amplitude at an observation point P located at angle θ from the center of the two slits reads

$$f(\theta) = A \sin\left(\frac{2\pi}{\lambda}l_1 - \omega t\right) + A \sin\left(\frac{2\pi}{\lambda}l_2 - \omega t\right), \quad (3)$$

$$\propto \cos\left(\frac{\pi l}{\lambda} \sin \theta t\right), \quad (4)$$

where l_1 and l_2 are the distance of the point P from each of the slits, and l is the distance between the slits (see the upper panel of Fig. 3). Here, we have used the fact that l is much smaller than the distance of P from the slits, L . Substituting this amplitude into Eq. (2), one obtains [18]

$$\Phi(X, Y) \propto \sigma(kY\Delta\varphi) \left\{ \sigma\left[\left(kX + \frac{kl}{2} \cos \theta_0\right)\Delta\theta\right] + \sigma\left[\left(kX - \frac{kl}{2} \cos \theta_0\right)\Delta\theta\right] \right\}, \quad (5)$$

where $k = 2\pi/\lambda$ is the wave length and the function $\sigma(x)$ is defined as $\sigma(x) = \sin x/x$. The lower panel of Fig. 3 shows $|\Phi(X, Y)|^2$ on the two-dimensional (X, Y) plane for

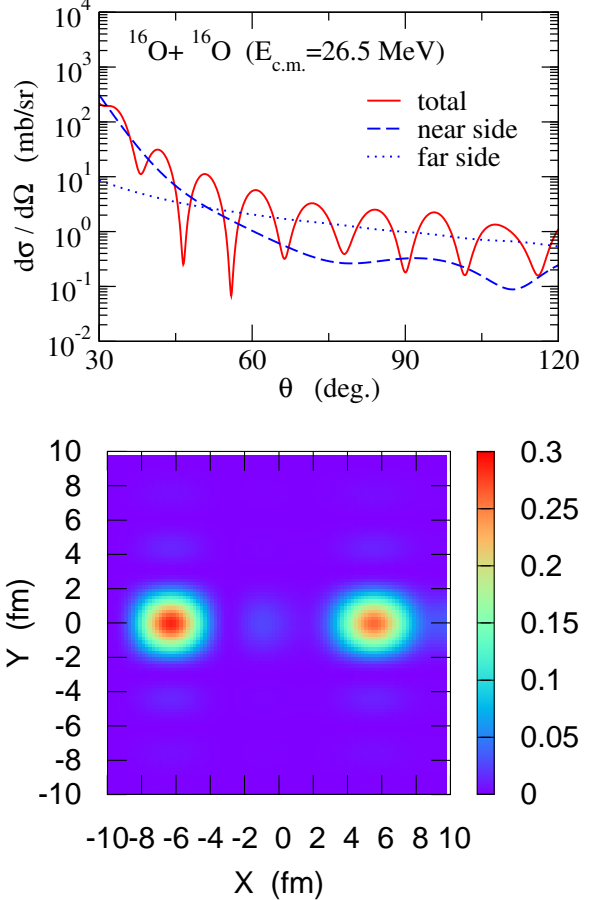


Figure 4. (Upper panel) Differential cross sections for $^{16}\text{O}+^{16}\text{O}$ elastic scattering at $E_{\text{c.m.}} = 26.5$ MeV obtained with the optical potential model. The anti-symmetrization between the projectile and the target nuclei is ignored for simplicity. The solid line shows the result of the optical potential model calculation, while the dashed and the dotted lines show its decomposition to the near-side and the far-side components, respectively. (Lower panel) The visualization of $^{16}\text{O}+^{16}\text{O}$ elastic scattering at $E_{\text{c.m.}} = 26.5$ MeV on a two-dimensional screen, whose coordinates are specified by X and Y . The left and the right peaks correspond to the far-side and the near-side components, respectively.

$l = 1, k = 30, \theta_0 = 0$, and $\Delta\theta = \Delta\varphi = 15$ degree. One can see that this function shows a double peaked structure, and thus Eq. (2) corresponds to making an image of the scattering waves onto a two-dimensional screen, whose coordinates are specified by X and Y . Notice that the function $\sigma(x)$ is peaked at $x = 0$, and thus Eq. (5) indicates that the peaks of $|\Phi(X, Y)|^2$ appear at $X = \pm \frac{kl}{2} \cos \theta_0$. This actually coincides with the peak position shown in Fig. 3. Notice that this method has been subsequently used to demonstrate that scattering of a string in the string theory is similar to a double slit problem [18].

Let us next apply the same method to heavy-ion elastic scattering [19, 20]. The upper panel of Fig. 4 shows differential cross sections for elastic scattering between two ^{16}O nuclei at $E_{\text{c.m.}} = 26.5$ MeV. The solid line shows the result of an optical potential model calculation, while the dashed and the dotted lines show its decomposition into the near-

side and the far-side components, respectively. See Ref. [19] for the actual values of the parameters in the optical potential. For simplicity, we have ignored the symmetrization of the colliding nuclei. The imaging of the scattering, $|\Phi(X, Y)|^2$, obtained with $\theta_0 = 55$ deg., $\Delta\theta = \Delta\varphi = 15$ deg. is shown in the lower panel of Fig. 4. One can see a clear two-peaked structure, as in the double slit problem. By decomposing the scattering amplitude into the near-side and the far-side components, it can be shown that the peak at positive values of X corresponds to the near-side component while the peak at negative values of X corresponds to the far-side component [19].

In this way, by visualizing heavy-ion reactions with the imaging technique presented here, one can gain an intuitive picture of quantum interference phenomena. An advantage of this method is that one can obtain an idea on how many different processes interfere with each other in a nuclear reaction process without explicitly decomposing the scattering amplitude. This property has been utilized in Ref. [20] to discuss the nearside-farside and the barrier-wave-internal-wave interferences in $\alpha+{}^{40}\text{Ca}$ scattering.

3 Multi-channel problems

3.1 Subbarrier enhancement of fusion cross sections

We next discuss multi-channel problems [21]. We in particular discuss the role of nuclear deformation in heavy-ion fusion reactions at energies around the Coulomb barrier [8, 21, 22]. A typical example is the ${}^{16}\text{O}+{}^{154}\text{Sm}$ fusion reaction, whose cross sections are shown in Fig. 5 as a function of the incident energy in the center of mass frame. Here the energy is measured with respect to the height of the Coulomb barrier, $V_b=60.35$ MeV, which is estimated with a typical Woods-Saxon potential. In the figure, the dashed line is obtained with the potential model by assuming an inert ${}^{154}\text{Sm}$. This calculation largely underestimates the fusion cross sections at energies below the barrier. ${}^{154}\text{Sm}$ is a typical deformed nucleus, and the large enhancement of fusion cross sections has been attributed to the deformation effect of ${}^{154}\text{Sm}$. In fact, by taking into account the deformation of ${}^{154}\text{Sm}$ with the orientation average formula [8, 21],

$$\sigma_{\text{fus}}(E) = \int_0^1 d(\cos \theta) \sigma_{\text{fus}}(E; \theta), \quad (6)$$

where θ is the orientation angle of ${}^{154}\text{Sm}$ with respect to the beam direction, and $\sigma_{\text{fus}}(E; \theta)$ is the fusion cross section for a fixed orientation angle, one obtains the solid line, which well reproduces the experimental fusion cross sections.

The orientation average formula, Eq. (6), can be derived as follows. For an axially deformed target nucleus, the total Hamiltonian of the system reads,

$$H = -\frac{\hbar^2}{2\mu} \nabla^2 + H_{\text{rot}} + V(r, \theta), \quad (7)$$

where μ is the reduced mass, r is the relative coordinate between the projectile and the target nuclei, and $V(r, \theta)$

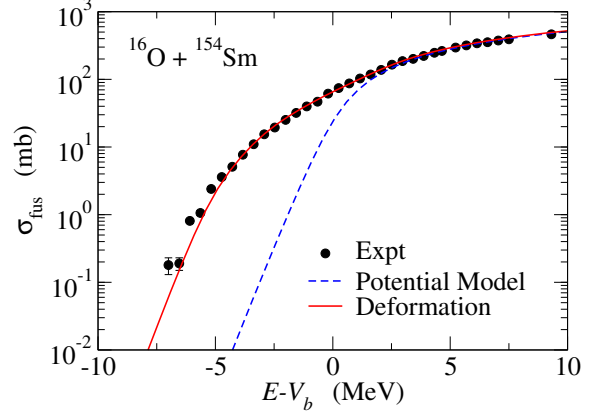


Figure 5. Fusion cross sections for the ${}^{16}\text{O}+{}^{154}\text{Sm}$ system as a function of the incident energy in the center of mass frame, which is measured with respect to the height of the Coulomb barrier, $V_b=60.35$ MeV. The dashed line is obtained with a single-channel calculation, while the solid line takes into account the deformation effect of the ${}^{154}\text{Sm}$ nucleus with the orientation average formula, Eq. (6). The experimental data are taken from Ref. [23].

is the angle dependent inter-nucleus potential. H_{rot} is the rotational energy of the target nucleus given by,

$$H_{\text{rot}} = \frac{\hat{I}^2 \hbar^2}{2\mathcal{J}} = -\frac{\hbar^2}{2\mathcal{J}} \left(\frac{1}{\sin \theta} \frac{\partial}{\partial \theta} \left(\sin \theta \frac{\partial}{\partial \theta} \right) + \frac{1}{\sin^2 \theta} \frac{\partial^2}{\partial \varphi^2} \right), \quad (8)$$

where \hat{I} is the angular momentum for the rotational motion of the deformed target nucleus, \mathcal{J} is the momentum inertia, and φ is the azimuthal angle. For the medium heavy nuclei, such as ${}^{154}\text{Sm}$, the rotational energies are much smaller than the typical energy scale of the reactions, and the rotational Hamiltonian H_{rot} may be neglected in the total Hamiltonian, (7). In this case, the total Hamiltonian is diagonal with respect to the angle θ . Since a small rotational energy corresponds to a large moment of inertia \mathcal{J} , the angle θ is frozen during the reaction. Since the wave function for the ground state of the rotational motion is given by $Y_{00}(\theta)$, the total fusion cross section is given as a weighted average of fusion cross sections for a fixed value of θ with the weight factor given by $|Y_{00}(\theta)|^2$. This leads to the orientation average formula given by Eq. (6).

In this adiabatic limit, the rotational motion is so small that the initial configuration is retained during the reaction. Since the ground state is given as a linear superposition of a deformed wave function with different orientations, the orientation average formula is nothing but taking a snapshot of a deformed nucleus. Notice that this does not mean that the deformed nucleus is not rotationally excited during the reaction. The truth is rather opposite: the nucleus is coherently excited to all the rotational states. Notice that, from the uncertainty principle, one needs to superpose all the angular momentum states if one would like to freeze the orientation angle, that is,

$$|\theta\rangle = \sum_{I=0}^{\infty} w(\theta)|I\rangle, \quad w(\theta) = \langle I|\theta\rangle. \quad (9)$$

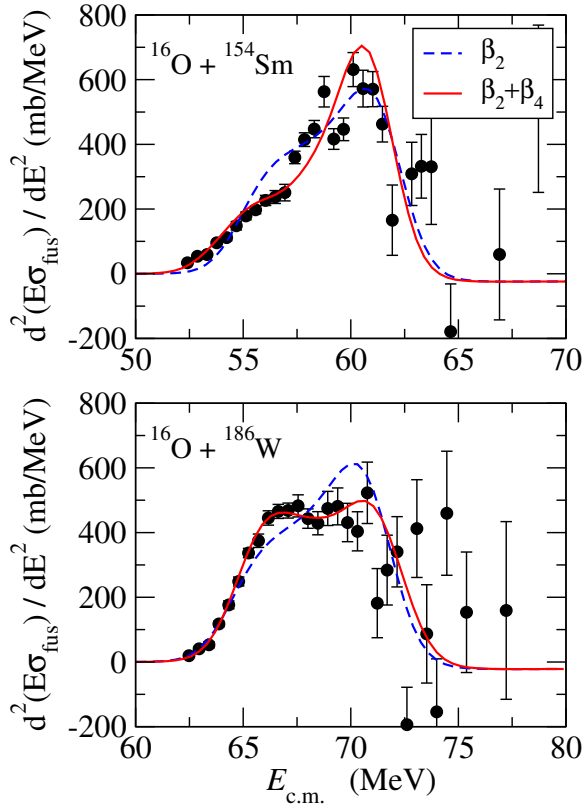


Figure 6. Fusion barrier distribution for the $^{16}\text{O}+^{154}\text{Sm}$ system (the upper panel) and for the $^{16}\text{O}+^{186}\text{W}$ system (the lower panel). The blue dashed lines take into account only the quadrupole deformation of the target nuclei, while the red solid lines takes into account in addition the hexadecapole deformation. The actual values of the deformation parameters are $(\beta_2, \beta_4) = (0.33, 0.05)$ for ^{154}Sm and $(\beta_2, \beta_4) = (0.29, -0.03)$ for ^{186}W . The experimental data are taken from Ref. [23].

In fact, the orientation average formula, Eq. (6), can be derived from the coupled-channels equations by neglecting the excitation energies of those states [21, 24].

3.2 Barrier distributions

In Ref. [25], Rowley, Satchler and Stelson proposed the so called fusion barrier distribution $D_{\text{fus}}(E)$, that is defined as

$$D_{\text{fus}}(E) = \frac{d^2(E\sigma_{\text{fus}})}{dE^2}. \quad (10)$$

For a single-channel problem, this function yields a Gaussian-like function centered at the barrier height energy [8, 9]. For a multi-channel problem, a single barrier is replaced by a multiple of barriers, and the barrier distribution (10) provides a way to visualize how these barriers are distributed. For instance, in Eq. (6), the barriers are specified for each value of θ , and these are distributed with the weight factor given by $\sin \theta$.

It has been demonstrated that the barrier distribution is sensitive to nuclear structure, especially to the sign of hexadecapole deformation parameter [9, 23]. For instance,

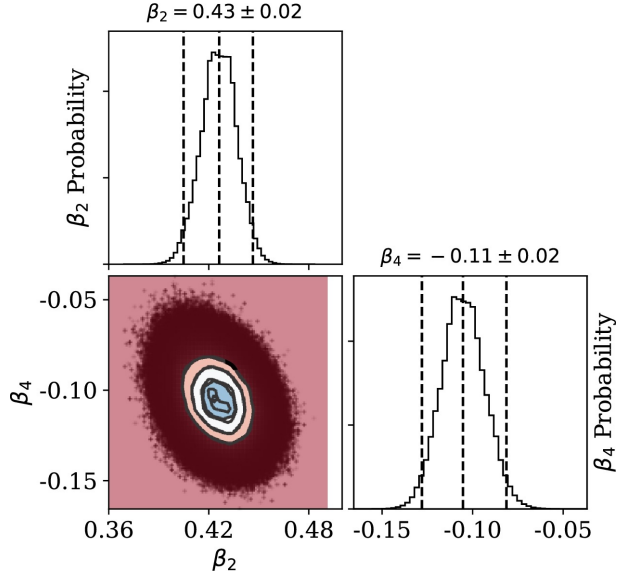


Figure 7. Multidimensional probability distributions of β_2 and β_4 for ^{24}Mg obtained with a Bayesian analysis of the quasi-elastic barrier distribution for the $^{24}\text{Mg}+^{90}\text{Zr}$ reaction. Taken from Ref. [26].

Fig. 6 compares the barrier distribution for the $^{16}\text{O}+^{154}\text{Sm}$ system with that for the $^{16}\text{O}+^{186}\text{W}$ system. One can clearly see that the shape of the barrier distribution is significantly different for these two systems. It is known that both ^{154}Sm and ^{186}W have a similar quadrupole deformation parameter to each other. The dashed lines in the figure show the barrier distributions with the quadrupole deformation parameter of each target nuclei. This calculation leads to similar barrier distributions to each other for these systems. The observed difference in the barrier distributions can be attributed to the hexadecapole deformation parameters, β_4 . While ^{154}Sm has a positive β_4 around $+0.05$, ^{186}W has a negative β_4 around -0.03 . The solid lines in Fig. 6 are obtained by taking into account both the quadrupole and the hexadecapole deformation parameters of the target nuclei. One can now see that the different shapes of the barrier distributions can be well reproduced. It is interesting to notice that the hexadecapole deformation is by about one order of magnitude smaller than the quadrupole deformation, but still the shape of the barrier distribution is significantly affected by the hexadecapole deformation. In this way, the barrier distribution reveal how potential barriers are distributed, proving a fingerprint of reaction dynamics as well as a powerful tool to extract information on the nuclear shapes.

Using this property of the barrier distributions, the deformation parameters of ^{24}Mg and ^{28}Si have been recently extracted with high precision [26, 27]. To this end, Refs. [26, 27] analyzed the barrier distributions derived from quasi-elastic scattering [28, 29] using a Bayesian analysis with coupled-channels calculations (see Fig. 7). The resultant values of the deformation parameters are $(\beta_2, \beta_4) = (0.43 \pm 0.02, -0.11 \pm 0.02)$ for ^{24}Mg and $(\beta_2, \beta_4) = (-0.38 \pm 0.01, 0.03 \pm 0.01)$ for ^{28}Si , which are with much higher precision than the previous deter-

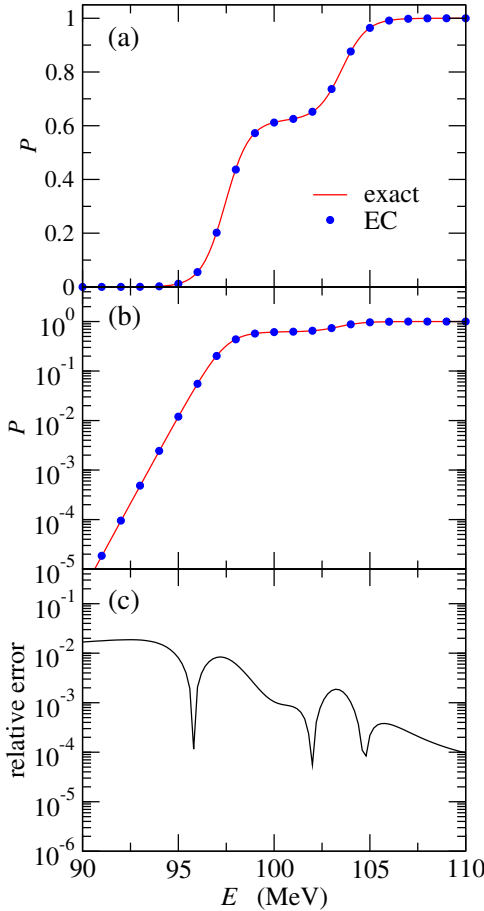


Figure 8. (a) The penetrability for a one-dimensional two-channel problem as a function of the energy E , plotted in the linear scale. The solid line shows the exact result, while the dashed line is obtained with the eigenvector continuation for the strength of the coupling potential. (b) The same as (a) but in the logarithmic scale. (c) The relative error defined by $|P_{\text{exact}} - P_{\text{EC}}|/P_{\text{exact}}$, where P_{exact} and P_{EC} are the exact penetrability and that obtained with the eigenvector continuation, respectively.

minations, e.g., with proton inelastic scattering. This once again indicates that the barrier distribution offers a powerful method to probe nuclear shapes.

3.3 Emulator for multi-channel scattering

In order to perform a Bayesian analysis presented in the last part of the previous subsection, one has to repeat coupled-channels calculations many times with different values of deformation parameters. This can be time-consuming if the number of channels included is large. In that situation, it is useful to have an emulator, which provides a good interpolation/extrapolation scheme to speed-up the calculations.

To construct an emulator, the eigenvector continuation (EC) has often been employed [30, 31]. In this method, one linearly superposes a few eigenvectors of the model Hamiltonian with several different model parameters. That

is, to solve the eigenvalue problem of a Hamiltonian $H(\theta)$,

$$H(\theta)|\Psi(\theta)\rangle = E(\theta)|\Psi(\theta)\rangle, \quad (11)$$

where θ is a parameter in the Hamiltonian, one constructs an approximate solution by taking

$$\Psi(\theta) = \sum_{i=1}^N c_i \Psi(\theta_i), \quad (12)$$

where $\Psi(\theta_i)$ is an eigenfunction of the Hamiltonian $H(\theta_i)$. Here, N is the number of the basis functions, and the coefficients $\{c_i\}$ are determined variationally. This method was firstly applied to bound-state problems of atomic nuclei, but it has recently been applied to nuclear reactions as well [32–34].

Figure 8 shows the penetrabilities for a one-dimensional two-channel Hamiltonian,

$$H = \begin{pmatrix} V(x) & F(x) \\ F(x) & V(x) + \epsilon \end{pmatrix}, \quad (13)$$

with a Gaussian barrier $V(x) = V_0 e^{-x^2/2s^2}$ and a Gaussian coupling form factor $F(x) = F_0 e^{-x^2/2s_f^2}$. The solid lines show the exact results with $V_0 = 100$ MeV, $F_0 = 3$ MeV, $s = s_f = 3$ fm, and $\epsilon = 1$ MeV, while the dots show the results of the eigenvector continuation with $F_{0i} = 1.5, 2.0, 2.5, 3.5$, and 4.5 MeV to simulate the solution for $F_0 = 3$ MeV [35]. To implement the eigenvector continuation, we use the discrete basis method combined with the Kohn variational principle [36]. One can clearly see that the eigenvector continuation well reproduces the exact results, both in the linear scale (the top panel) and in the logarithmic scale (the middle panel). In particular, the exponential energy dependence of the penetrability at energies well below the barrier is successfully reproduced. The relative error is shown in the bottom panel, indicating that the eigenvector continuation reproduces the exact result within about 10^{-4} at energies above the barrier, even though the error increases to $O(10^{-2})$ at energies below the barrier.

4 Relativistic Heavy-ion Collisions

Let us lastly discuss relativistic heavy-ion collisions, for which there have been increasing interests in recent years in connection to a probe for nuclear deformations [10, 11]. An idea of this approach is that the time (the energy) scale of heavy-ion collisions is much smaller (larger) at relativistic energies than the time (the energy) scale of nuclear motions, such that one can take a snapshot of a nucleus by choosing the central collision region where the projectile and the target nuclei significantly overlap with each other. In other words, the adiabatic approximation works well in the relativistic heavy-ion collisions, and the initial nuclear configuration is frozen during a collision, as in heavy-ion fusion reactions of a deformed nucleus discussed in Sec. 3. Using this property, the recent STAR collaborations successfully extracted the deformation parameter of ^{238}U to be $\beta_2 = -0.286 \pm 0.025$ and $\gamma = 8.7 \pm 4.8^\circ$ [37].

One of the main interests in nuclear structure physics is how to distinguish a static deformation from a dynamical deformation, that is, surface vibrations of *spherical* nuclei. In this connection, we mention that sub-barrier fusion reaction is significantly affected not only by a static deformation of deformed nuclei but also by a dynamical deformation of spherical nuclei [38]. Moreover they lead to considerably different fusion barrier distributions from each other [8, 9, 21]. It would be interesting if this is the case also for relativistic heavy-ion collisions. To examine this, we particularly discuss the eccentricity parameter of the density distribution for the initial condition of relativistic heavy-ion collisions. Here, the eccentricity parameter is defined with the polar coordinate (r, θ, ϕ) as

$$\epsilon_n \equiv -\frac{\int d\mathbf{r} r^n \sin^n \theta e^{in\phi} \rho(\mathbf{r})}{\int d\mathbf{r} r^n \sin^n \theta \rho(\mathbf{r})} = -\frac{\langle (x - iy)^n \rangle}{\langle (x^2 + y^2)^{n/2} \rangle}. \quad (14)$$

To this end, we take the beam direction of a collision for the z -axis in the space-fixed coordinate system and assume for simplicity a central collision such that the projectile and the target nuclei have a complete overlap. It has been well recognized that the eccentricity parameter ϵ_n is directly correlated with the final-state anisotropic flows, v_n , for ultra-central collisions [11, 37].

To compute the eccentricity parameter (14), we shall employ a deformed Woods-Saxon density for $\rho(\mathbf{r})$ given by

$$\rho(\mathbf{r}) = \frac{\rho_0}{1 + e^{(r-R(\theta,\phi))/a}}, \quad (15)$$

where ρ_0 and a are the central density and the diffuseness parameter, respectively. Here, $R(\theta, \phi)$ is the angle dependent radius given by

$$R(\theta, \phi) = R_0 \left(1 - \frac{1}{4\pi} \sum_{\lambda, \mu} |\alpha_{\lambda\mu}|^2 + \sum_{\lambda, \mu} \alpha_{\lambda\mu} Y_{\lambda\mu}^*(\hat{\mathbf{r}}) \right), \quad (16)$$

where R_0 is the radius parameter. In this equation, the second term in the parenthesis is due to the volume conservation, and $\alpha_{\lambda\mu}$ is the deformation parameter in the space-fixed system satisfying the condition $\alpha_{\lambda\mu}^* = (-1)^\mu \alpha_{\lambda, -\mu}$ [39].

In the harmonic oscillator model for spherical nuclei, the deformation parameter $\alpha_{\lambda\mu}$ acts as a coordinate of the harmonic oscillator. The classical Hamiltonian for the vibration reads

$$H = \frac{1}{2} \sum_{\lambda, \mu} \left(B_\lambda |\dot{\alpha}_{\lambda\mu}|^2 + C_\lambda |\alpha_{\lambda\mu}|^2 \right), \quad (17)$$

where the dot denotes the time derivative, and B_λ and C_λ are the inertia and the stiffness parameters of the oscillator, respectively. Notice that, for a given λ , there exist $2\lambda + 1$ independent harmonic oscillators with $\{\alpha_{\lambda\mu}\}$ as the coordinates. In quantum mechanics, the ground state of these harmonic oscillators has the zero point fluctuation, with the probability distribution of the coordinate given by,

$$P(x) = \frac{1}{\sqrt{2\pi\sigma_\lambda^2}} e^{-x^2/(2\sigma_\lambda^2)}, \quad (18)$$

where σ_λ is the amplitude of the zero point motion, given by $\sigma_\lambda = \sqrt{\hbar/(2B_\lambda\omega_\lambda)}$ with $\omega_\lambda = \sqrt{C_\lambda/B_\lambda}$. The expectation value of the absolute square of the eccentricity parameter is then evaluated as,

$$\langle |\epsilon_n|^2 \rangle = \int \left(\prod_{\lambda, \mu} d\alpha_{\lambda\mu} P(\alpha_{\lambda\mu}) \right) |\epsilon_n(\{\alpha_{\lambda\mu}\})|^2, \quad (19)$$

where $\epsilon_n(\{\alpha_{\lambda\mu}\})$ is the eccentricity parameter (14) for a given set of $\{\alpha_{\lambda\mu}\}$. With the probability distribution given by Eq. (18), the expectation value of $\sum_\lambda |\alpha_{\lambda\mu}|^2$ is computed as

$$\left\langle \sum_\mu |\alpha_{\lambda\mu}|^2 \right\rangle = (2\lambda + 1)\sigma_\lambda^2 \equiv (\beta_\lambda)^2. \quad (20)$$

In low-energy heavy-ion fusion reactions, the square root of this quantity is often referred to as the (dynamical) deformation parameter and is denoted by β_λ [8, 21]. The value of the dynamical deformation parameter can be estimated from a measured electronic transition probability $B(E\lambda) \uparrow$ from the ground state of a spherical nucleus to an excited state as [8, 21],

$$\beta_\lambda = \frac{4\pi}{3ZR_0^4} \sqrt{\frac{B(E\lambda) \uparrow}{e^2}}, \quad (21)$$

where Z is the atomic number of the nucleus.

On the other hand, in the case of static deformation, one usually transforms the coordinate system to the body-fixed system with an appropriate choice of principle axes. For an axially-symmetric shape, this leads to [40]

$$\alpha_{\lambda\mu} = \beta_\lambda D_{0\mu}^\lambda(\Omega), \quad (22)$$

where $D_{\mu'\mu}^\lambda$ is the Wigner D function and Ω is the Euler angle for the transformation from the body-fixed to the space-fixed frames. By substituting this expression into Eq. (16), one can evaluate the eccentricity parameter $\epsilon_n(\Omega)$ for a given Euler angle Ω . The average value of the absolute square of the eccentricity parameter reads,

$$\langle |\epsilon_n|^2 \rangle = \int \frac{d\Omega}{8\pi^2} |\epsilon_n(\Omega)|^2. \quad (23)$$

Figure 9 compares the distribution of the eccentricity parameters for the surface vibration (SV) with that for the static deformation (SD) for $^{58}\text{Ni}+^{58}\text{Ni}$ collision. To this end, we generate $\{\alpha_{\lambda\mu}\}$ randomly according to the probability distribution in Eq. (18) for SV, while for SD only Ω is randomly sampled with fixed β_λ for the axial shape. The value of β_2 is estimated to be 0.218 from the measured $B(E2)$ for the transition from the ground state to the first 2^+ state at 1.45 MeV in ^{58}Ni . One can clearly see in the figure that SV and SD lead to significantly different distributions of the eccentricity parameters from each other, despite that the mean values are similar to each other, that is, $\langle |\epsilon_2| \rangle$ is 0.112 and 0.119 for SV and SD, respectively. This becomes even clearer if the eccentricity parameter for each sample is plotted as a function of the root mean square radius on the perpendicular plane, $r_\perp \equiv \sqrt{\langle x^2 + y^2 \rangle}$, as is shown in Fig. 10.

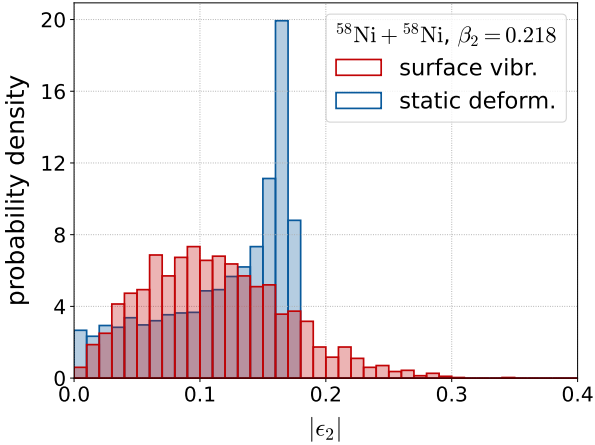


Figure 9. Probability densities of the quadrupole eccentricity parameter $|\epsilon_2|$ for the $^{58}\text{Ni} + ^{58}\text{Ni}$ collision. The red and blue colors denote the results for the surface vibration and the static deformation, respectively.

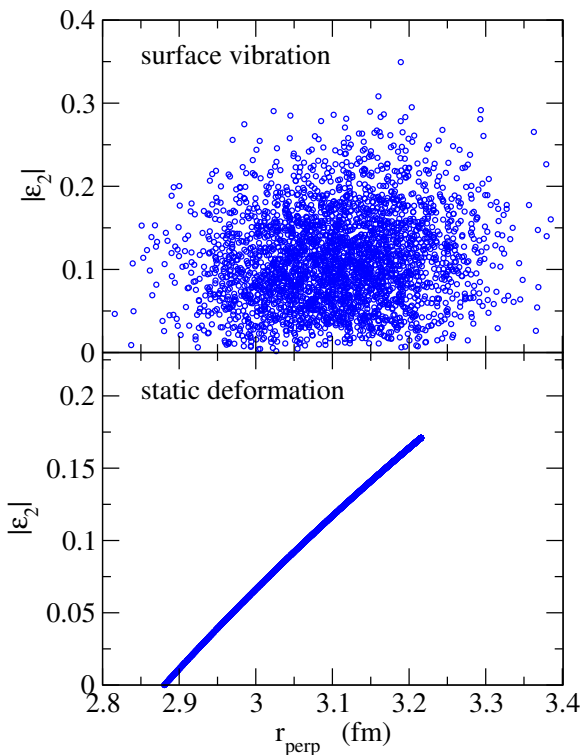


Figure 10. The distributions of the quadrupole eccentricity parameters ϵ_2 for the $^{58}\text{Ni} + ^{58}\text{Ni}$ collision plotted as a function of the root mean square radius on the perpendicular plane, $r_\perp \equiv \sqrt{\langle x^2 + y^2 \rangle}$.

These suggest that relativistic heavy-ion collisions provide an interesting way to distinguish between dynamical deformations (i.e., surface fluctuations) and static deformations of atomic nuclei.

5 Summary

We have discussed the dynamics of low-energy heavy-ion reactions. We first used the optical potential model and demonstrated that a part of the imaginary part of an optical potential can be well modeled with a simple model that consists of a random matrix for a compound nucleus. By changing the level density and the decay width of the compound nucleus states, the model can describe both the overlapping resonance regime and the isolated resonance regime, as in the fusion cross sections of the $^{12}\text{C} + ^{12}\text{C}$ and $^{12}\text{C} + ^{13}\text{C}$ systems. We next introduced the imaging technique for heavy-ion elastic scattering. This is to take the Fourier transform of the scattering amplitude. We have shown that this yields an intuitive view of quantum interference phenomena in heavy-ion reactions, such as a nearside-farside interference and a barrier-wave-internal-wave interference.

We then discussed multi-channel problems, putting some emphasis on heavy-ion fusion reactions at subbarrier energies. It has been well known that fusion cross sections are largely enhanced at these energies due to collective excitations of colliding nuclei, such as the rotational excitations of a deformed nucleus and the surface vibrations of a spherical nucleus. Using fusion barrier distributions, the deformation parameters have been successfully extracted for several nuclei. For such analyses, one needs to carry out coupled-channels calculations many times for different values of deformation parameters. We have demonstrated that an emulator for multi-channel scattering provides a powerful tool for that purpose.

Lastly, we have discussed relativistic heavy-ion collisions from the viewpoint of probing nuclear shapes. By computing the eccentricity parameters, we have demonstrated that a surface vibration and a static deformation lead to considerably different distributions of the eccentricity parameters. This suggests that relativistic heavy-ion collisions may provide a promising tool to distinguish between a static deformation and a dynamical deformation, making a good intersection between low-energy and high-energy nuclear physics.

All these studies strongly demonstrate that nuclear reaction dynamics is rich and intriguing to study. This all comes from the fact that atomic nuclei are composite quantum many-body systems and, as a consequence, there is a strong interplay between nuclear structure and nuclear reactions. This has been known well in low-energy nuclear reactions, but recent studies on relativistic heavy-ion collisions have revealed that this is the case also in high-energy nuclear collisions. We are now at an interesting stage to further explore nuclear reaction dynamics across a wide range of energy scales.

Acknowledgment

We thank G.F. Bertsch, Y. Gupta, K. Heo, M. Kimura, M. Kitazawa, Z. Liao, K. Uzawa, T. Yoda, S. Yoshida for collaborations. This work was partly supported by JSPS KAKENHI Grant Number JP23K03414.

References

- [1] T. Wakasa, K. Ogata, T. Noro, Proton-induced knockout reactions with polarized and unpolarized beams, *Prog. in Part. and Nucl. Phys.* **96**, 32 (2017). <https://doi.org/10.1016/j.ppnp.2017.06.002>
- [2] K. Sekiguchi, Y. Wada, J. Miyazaki, H. Witała, M. Dozono, U. Gebauer, J. Golak, H. Kamada, S. Kawase, Y. Kubota et al., Complete set of deuteron analyzing powers for dp elastic scattering at 250–294 mev/nucleon and the three-nucleon force, *Phys. Rev. C* **89**, 064007 (2014). [10.1103/PhysRevC.89.064007](https://doi.org/10.1103/PhysRevC.89.064007)
- [3] S. Hofmann, G. Münzenberg, The discovery of the heaviest elements, *Rev. Mod. Phys.* **72**, 733 (2000). [10.1103/RevModPhys.72.733](https://doi.org/10.1103/RevModPhys.72.733)
- [4] Y. Oganessian, V. Utyonkov, Superheavy nuclei from ^{48}Ca -induced reactions, *Nucl. Phys. A* **944**, 62 (2015), special Issue on Superheavy Elements. <https://doi.org/10.1016/j.nuclphysa.2015.07.003>
- [5] G.E. Mitchell, A. Richter, H.A. Weidenmüller, Random matrices and chaos in nuclear physics: Nuclear reactions, *Rev. Mod. Phys.* **82**, 2845 (2010). [10.1103/RevModPhys.82.2845](https://doi.org/10.1103/RevModPhys.82.2845)
- [6] H. Hofmann, The Physics of Warm Nuclei: with Analogies to Mesoscopic Systems (Oxford University Press, 2008), ISBN 9780198504016, <https://doi.org/10.1093/acprof:oso/9780198504016.001.0001>
- [7] A.B. Balantekin, N. Takigawa, Quantum tunneling in nuclear fusion, *Rev. Mod. Phys.* **70**, 77 (1998). [10.1103/RevModPhys.70.77](https://doi.org/10.1103/RevModPhys.70.77)
- [8] K. Hagino, N. Takigawa, Subbarrier fusion reactions and many-particle quantum tunneling, *Prog. Theo. Phys.* **128**, 1061 (2012). [10.1143/PTP.128.1061](https://doi.org/10.1143/PTP.128.1061)
- [9] M. Dasgupta, D.J. Hinde, N. Rowley, A.M. Stefanini, Measuring barriers to fusion, *Ann. Rev. of Nucl. and Part. Sci.* **48**, 401 (1998). <https://doi.org/10.1146/annurev.nucl.48.1.401>
- [10] J. Jia, G. Giacalone, B. Bally, J.D. Brandenburg, U. Heinz, S. Huang, D. Lee, Y.J. Lee, C. Loizides, W. Li et al., Imaging the initial condition of heavy-ion collisions and nuclear structure across the nuclide chart, *Nucl. Sci. and Tech.* **35**, 220 (2024). [10.1007/s41365-024-01589-w](https://doi.org/10.1007/s41365-024-01589-w)
- [11] T. STAR Collaboration, Imaging nuclear shape through anisotropic and radial flow in high-energy heavy-ion collisions, *Rep. on Prog. in Phys.* **88**, 108601 (2025). [10.1088/1361-6633/ae0fc3](https://doi.org/10.1088/1361-6633/ae0fc3)
- [12] D. Hinde, M. Dasgupta, E. Simpson, Experimental studies of the competition between fusion and quasi-fission in the formation of heavy and superheavy nuclei, *Prog. in Part. and Nucl. Phys.* **118**, 103856 (2021). <https://doi.org/10.1016/j.ppnp.2021.103856>
- [13] N. Zhang, X. Wang, D. Tudor, B. Bucher, I. Burducea, H. Chen, Z. Chen, D. Chesneanu, A. Chilug, L. Gasques et al., Constraining the $^{12}\text{C}+^{12}\text{C}$ astrophysical s-factors with the $^{12}\text{C}+^{13}\text{C}$ measurements at very low energies, *Phys. Lett. B* **801**, 135170 (2020). <https://doi.org/10.1016/j.physletb.2019.135170>
- [14] C.L. Jiang, B.B. Back, H. Esbensen, R.V.F. Janssens, K.E. Rehm, R.J. Charity, Origin and consequences of $^{12}\text{C}+^{12}\text{C}$ fusion resonances at deep sub-barrier energies, *Phys. Rev. Lett.* **110**, 072701 (2013). [10.1103/PhysRevLett.110.072701](https://doi.org/10.1103/PhysRevLett.110.072701)
- [15] K. Hagino, Simple schematic model for transmission coefficients in the isolated resonance region, *Phys. Rev. C* **112**, 034611 (2025). [10.1103/s63h-y87h](https://doi.org/10.1103/s63h-y87h)
- [16] D.A. Bromley, J.A. Kuehner, E. Almqvist, Elastic scattering of identical spin-zero nuclei, *Phys. Rev.* **123**, 878 (1961). [10.1103/PhysRev.123.878](https://doi.org/10.1103/PhysRev.123.878)
- [17] M. Hussein, K. McVoy, Nearside and farside: The optics of heavy ion elastic scattering, *Prog. in Part. and Nucl. Phys.* **12**, 103 (1984). [https://doi.org/10.1016/0146-6410\(84\)90003-6](https://doi.org/10.1016/0146-6410(84)90003-6)
- [18] K. Hashimoto, Y. Matsuo, T. Yoda, String is a double slit, *Prog. Theor. Exp. Phys.* **2023**, 043B04 (2023). [10.1093/ptep/ptad045](https://doi.org/10.1093/ptep/ptad045)
- [19] K. Hagino, T. Yoda, Visualizing quantum coherence and decoherence in nuclear reactions, *Phys. Lett. B* **848**, 138326 (2024). <https://doi.org/10.1016/j.physletb.2023.138326>
- [20] K. Heo, K. Hagino, Visualization of quantum interferences in heavy-ion elastic scattering, *Phys. Rev. C* **111**, 034612 (2025). [10.1103/PhysRevC.111.034612](https://doi.org/10.1103/PhysRevC.111.034612)
- [21] K. Hagino, K. Ogata, A. Moro, Coupled-channels calculations for nuclear reactions: From exotic nuclei to superheavy elements, *Prog. in Part. and Nucl. Phys.* **125**, 103951 (2022). <https://doi.org/10.1016/j.ppnp.2022.103951>
- [22] K. Hagino, N. Rowley, A. Kruppa, A program for coupled-channel calculations with all order couplings for heavy-ion fusion reactions, *Comput. Phys. Comm.* **123**, 143 (1999). [https://doi.org/10.1016/S0010-4655\(99\)00243-X](https://doi.org/10.1016/S0010-4655(99)00243-X)
- [23] J.R. Leigh, M. Dasgupta, D.J. Hinde, J.C. Mein, C.R. Morton, R.C. Lemmon, J.P. Lestone, J.O. Newton, H. Timmers, J.X. Wei et al., Barrier distributions from the fusion of oxygen ions with $^{144,148,154}\text{Sm}$ and ^{186}W , *Phys. Rev. C* **52**, 3151 (1995). [10.1103/PhysRevC.52.3151](https://doi.org/10.1103/PhysRevC.52.3151)
- [24] M.A. Nagarajan, A.B. Balantekin, N. Takigawa, Geometric interpretation of the adiabatic model for heavy-ion fusion, *Phys. Rev. C* **34**, 894 (1986). [10.1103/PhysRevC.34.894](https://doi.org/10.1103/PhysRevC.34.894)
- [25] N. Rowley, G. Satchler, P. Stelson, On the “distribution of barriers” interpretation of heavy-ion fusion, *Phys. Lett. B* **254**, 25 (1991). [https://doi.org/10.1016/0370-2693\(91\)90389-8](https://doi.org/10.1016/0370-2693(91)90389-8)
- [26] Y. Gupta, B. Nayak, U. Garg, K. Hagino, K. Howard, N. Sensharma, M. Şenyiğit, W. Tan, P. O’Malley, M. Smith et al., Determination of

- hexadecapole (β_4) deformation of the light-mass nucleus ^{24}Mg using quasi-elastic scattering measurements, Phys. Lett. B **806**, 135473 (2020). <https://doi.org/10.1016/j.physletb.2020.135473>
- [27] Y. Gupta, V. Katariya, G. Prajapati, K. Hagino, D. Patel, V. Ranga, U. Garg, L. Danu, A. Pal, B. Joshi et al., Precise determination of quadrupole and hexadecapole deformation parameters of the sd-shell nucleus, ^{28}Si , Phys. Lett. B **845**, 138120 (2023). <https://doi.org/10.1016/j.physletb.2023.138120>
- [28] H. Timmers, J. Leigh, M. Dasgupta, D. Hinde, R. Lemmon, J. Mein, C. Morton, J. Newton, N. Rowley, Probing fusion barrier distributions with quasi-elastic scattering, Nucl. Phys. A **584**, 190 (1995). [https://doi.org/10.1016/0375-9474\(94\)00521-N](https://doi.org/10.1016/0375-9474(94)00521-N)
- [29] K. Hagino, N. Rowley, Large-angle scattering and quasielastic barrier distributions, Phys. Rev. C **69**, 054610 (2004). [10.1103/PhysRevC.69.054610](https://doi.org/10.1103/PhysRevC.69.054610)
- [30] D. Frame, R. He, I. Ipsen, D. Lee, D. Lee, E. Rrapaj, Eigenvector continuation with subspace learning, Phys. Rev. Lett. **121**, 032501 (2018). [10.1103/PhysRevLett.121.032501](https://doi.org/10.1103/PhysRevLett.121.032501)
- [31] T. Duguet, A. Ekström, R.J. Furnstahl, S. König, D. Lee, Colloquium: Eigenvector continuation and projection-based emulators, Rev. Mod. Phys. **96**, 031002 (2024). [10.1103/RevModPhys.96.031002](https://doi.org/10.1103/RevModPhys.96.031002)
- [32] R. Furnstahl, A. Garcia, P. Millican, X. Zhang, Efficient emulators for scattering using eigenvector continuation, Phys. Lett. B **809**, 135719 (2020). <https://doi.org/10.1016/j.physletb.2020.135719>
- [33] C. Drischler, M. Quinonez, P. Giuliani, A. Lovell, F. Nunes, Toward emulating nuclear reactions using eigenvector continuation, Phys. Lett. B **823**, 136777 (2021). <https://doi.org/10.1016/j.physletb.2021.136777>
- [34] J. Liu, J. Lei, Z. Ren, A complex scaling method for efficient and accurate scattering emulation in nuclear reactions, Phys. Lett. B **858**, 139070 (2024). <https://doi.org/10.1016/j.physletb.2024.139070>
- [35] K. Hagino, Z. Liao, S. Yoshida, M. Kimura, K. Uzawa, Emulating multichannel scattering based on eigenvector continuation in the discrete-basis formalism, Phys. Rev. C **112**, 024618 (2025). [10.1103/zpsz-7jld](https://doi.org/10.1103/zpsz-7jld)
- [36] K. Hagino, G.F. Bertsch, Role of momentum in the generator-coordinate method applied to barrier penetration, Phys. Rev. C **110**, 054610 (2024). [10.1103/PhysRevC.110.054610](https://doi.org/10.1103/PhysRevC.110.054610)
- [37] M.I. Abdulhamid et al. (STAR Collaboration), Imaging shapes of atomic nuclei in high-energy nuclear collisions, Nature **635**, 67 (2024). [10.1038/s41586-024-08097-2](https://doi.org/10.1038/s41586-024-08097-2)
- [38] H. Esbensen, Fusion and zero-point motions, Nucl. Phys. A **352**, 147 (1981). [https://doi.org/10.1016/0375-9474\(81\)90565-0](https://doi.org/10.1016/0375-9474(81)90565-0)
- [39] P. Ring, P. Schuck, The Nuclear Many-Body Problem (Springer Verlag, New York, 1980)
- [40] K. Hagino, M. Kitazawa, Probing surface vibrations of spherical nuclei in relativistic heavy-ion collisions, Phys. Rev. C **112**, L041901 (2025). [10.1103/2f3s-2nyn](https://doi.org/10.1103/2f3s-2nyn)